Geophysical Journal International

*Geophys. J. Int.* (2009) **179,** 1537–1546 doi: 10.1111/j.1365-246X.2009.04390.x

# Lithosphere–atmosphere–ionosphere coupling after the 2003 explosive eruption of the Soufriere Hills Volcano, Montserrat

Thomas Dautermann,[1]* Eric Calais,[2] Philippe Lognonné[3] and Glen S. Mattioli[4]

[1] *Purdue University, Department of Physics, West Lafayette,* IN 47907, *USA. E-mail: thomas.dautermann@dlr.de*
[2] *Purdue University, Department of Earth and Atmospheric Sciences, West Lafayette,* IN 47907, *USA*
[3] *Institut de Physique du Globe de Paris, Université Paris Diderot, Paris, France*
[4] *University of Arkansas, Department of Geosciences, Fayetteville,* AR 72701, *USA*

Accepted 2009 September 17. Received 2009 September 17; in original form 2008 July 7

## SUMMARY

Resonant coupling between the Earth and the atmosphere at frequencies where the solid Earth modes overlap the fundamental modes of the atmosphere allows for the triggering of oscillatory acoustic perturbations by ground excitation and vice versa. Here, we describe oscillatory perturbations observed in the solid Earth (from volumetric borehole strainmeter data) and in the atmosphere (from GPS-derived ionospheric total electron content) following the 2003 July 13, Soufrière Hills Volcano explosion (Montserrat, Lesser Antilles). Spectral analysis shows an amplitude peak at 4 mHz for both data sets, with similar waveforms and signal duration. Using a normal mode summation technique, we show that both signals are explained by a single explosive source in the atmosphere. Similarities in waveforms, in particular a double wave train also reported after several other explosion-triggered atmospheric perturbations, result from the superposition of the dominant (fundamental) atmospheric modes that trigger resonant coupling with the solid Earth around 4 mHz.

**Key words:** Numerical approximations and analysis; Ionosphere/atmosphere interactions; Volcano seismology; Acoustic properties; Dynamics of lithosphere and mantle; Explosive volcanism.



## 1 INTRODUCTION

Impulsive vertical displacements of the Earth surface from shallow earthquakes, explosions, seismic surface waves and tsunamis are known to trigger pressure waves in the atmosphere (e.g. Fitzgerald 1997; Calais *et al.* 1998; Afraimovich *et al.* 2001; Ducic *et al.* 2003; Artru *et al.* 2004; Occhipinti *et al.* 2006). Conversely, atmospheric sources such as nuclear or volcanic explosions can trigger seismic waves in the solid Earth. Widmer & Zürn (1992), for example, described long-period seismic waves (∼4 mHz) at global seismic stations following the 1982 April 4, El Chichon and the 1991 June 15, Mt Pinatubo volcanic explosions. The Pinatubo explosion was also also studied by Kanamori & Mori (1992), who found a bichromatic signal in the Rayleigh seismic wave at 3.7 and 4.3 mHz following the event. Based on the timing of these waves and the lack of global earthquake capable of generating the observed signals, these authors proposed that ground motion was caused by mechanical coupling between the solid Earth and the atmosphere pressure wave caused by the volcanic explosion.

The theory that quantitatively links atmospheric and solid Earth motions was first explored by Kanamori *et al.* (1994), who showed that volcanic explosions excite atmospheric oscillations in the frequency band of seismic Rayleigh surface waves. It was further developed by Watada (1995), who adapted the normal mode approach used in seismology to include the atmosphere and showed that resonant coupling occurs between the solid Earth and the atmosphere when their modes overlap in the frequency–wavenumber domain. Lognonné *et al.* (1998) extended this approach with a theory for seismogram summation, while Kobayashi (2007) developed additional numerical methods for mode calculation. This theory has been used to compute ionospheric signals associated to seismic waves, after the inclusion of the viscosity effects by Artru *et al.* (2001) and comparison with digital Doppler ionospheric data by Artru *et al.* (2004). This refinement is however not necessary for the modeling of the excitation of seismic waves by low altitude atmospheric sources, and Lognonné *et al.* (1998) were able to show that the bichromatic signal described by Kanamori & Mori (1992) in seismic waves after the 1991 Pinatubo explosion corresponded to the $l = 28$ and 34–37 modes. Lognonné (2009) also showed that the waveform of the Pinatubo eruption was well explained by an atmospheric source, located either near the ground or at 20–28 km of altitude, with a preference for a high altitude source corresponding to the blow-off of the volcanic eruption plume shock wave.

Although the theory is now well established, observations of solid Earth motion induced by atmospheric sources are scarce because the excitation of Rayleigh waves by the atmosphere is weak in the

*Now at the German Aerospace Center (DLR), Institute of Communication and Navigation, 82234 Wessling, Germany.

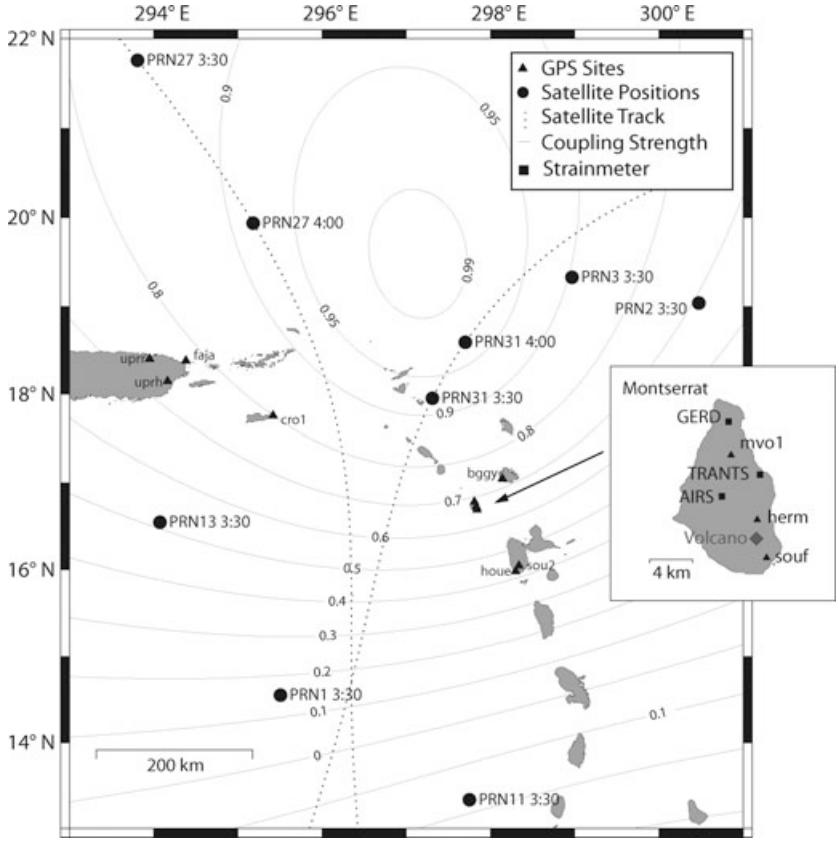


**Figure 1.** Map of the northeastern Caribbean showing the GPS sites (triangles) and CALIPSO borehole strainmeters (squares) used in this study. Dotted lines show the subionospheric point (SIP) traces for GPS satellites PRN27 and PRN31. Black circles mark the SIP of the satellites visible at the time of the explosion (with corresponding UT time indicated). Thin solid lines labeled from 0 to 1 are contours of the cosine of the angle between the acoustic ray direction and the magnetic field vector, a proxy for the efficiency of the neutral pressure wave at displacing free electrons (e.g. Dautermann *et al.* 2009). Note that only PRN27 and PRN31 are in areas of high coupling after the explosion.

far field. Near field observations should be much more sensitive, as they also record the excitation of the seismic near field signal by the atmospheric source, including the seismic signals generated by the coupling of the atmospheric acoustic waves with the seismic body waves. Although the explosive lava dome collapse of the Soufriere Hills Volcano (SHV) in 2003 on Montserrat was much less energetic thank previously studied volcanic explosions (volcano explosivity index of 3 (Herd *et al.* 2005) compared to 6 for Mt Pinatubo), the island and its surrounding were well instrumented with continuous GPS and strainmeters (Mattioli *et al.* 2004). This event therefore provides us with a unique opportunity to study the atmospheric pressure wave caused by the explosion and its potential effects both in the solid Earth and in the atmosphere. Dautermann *et al.* (2009) identified the acoustic perturbation caused by the explosion through the induced variations of ionospheric total electron content (TEC) derived from GPS measurements, modelled its propagation, and estimated the acoustic energy released by the explosion.

Here we show that signals recorded at borehole strainmeters on the island of Montserrat (Mattioli *et al.* 2004) following the SHV explosion have a frequency content and waveform remarkably similar to the atmospheric perturbation revealed in the GPS-TEC data. We use the normal mode summation technique developed by Watada (1995) and Lognonné *et al.* (1998) to test whether an explosion source can explain both the GPS-TEC and strainmeter observations, and whether acoustic energy leakage from the atmosphere back to the solid Earth can explain the observed volumetric strain signal.

## 2 DATA AND OBSERVATIONS

The SHV on Montserrat, Lesser Antilles (Fig. 1), erupted on 2003 July 13 in a sequence of events that led, at 3:35 UTC, to a large explosion and the collapse of the $210 \times 10^6\,\mathrm{m}^3$ volcanic dome (Herd *et al.* 2005). At the time, Montserrat was instrumented with Sacks–Evertson borehole dilatometers measuring volumetric strain and dual-frequency GPS stations as part of the Caribbean Andesite Lava Island Precision Seismo-geodetic Observatory (CALIPSO; Mattioli *et al.* 2004). Additionally, data from six permanent GPS receivers within 600 km of Montserrat were also available.

We take advantage of the fact that the differential delay between the GPS phase observables $\Phi_1$ and $\Phi_2$ on the two GPS frequencies is proportional to the integral of electron density along the GPS signal ray path to compute the TEC using

$$\mathrm{TEC} = \left[\Phi_2 - \frac{f_2}{f_1}\Phi_1 + N + f_2(b_r + b_s)\right] \frac{f_1^2 f_2}{f_1^2 - f_2^2} \frac{c}{A}, \qquad (1)$$

(e.g. Klobuchar 1985; Lognonné *et al.* 2006) where $f_1 = 1575.42$ MHz and $f_2 = 1227.6$ MHz are the two GPS carrier frequencies, $A = 40.3\,\mathrm{m}^3\,\mathrm{s}^{-2}$ and $c$ is the speed of light. $N$ is the phase ambiguity and can be derived from pseudo-range data. $b_r$ and $b_s$ are code delays specific to receiver and satellite hardware. These parameters can be estimated from the GPS data (Sardon *et al.* 1994; Mazzella *et al.* 2002), but they will be neglected here because these biases are constant over the time period of our observations

and we are only interested in short-term temporal variations of TEC. Each TEC measurement is associated with a subionospheric point (SIP), defined as the ground projection of the intersection between the receiver-satellite line-of-sight and the peak electron density height (325 km). TEC is commonly expressed in TECU (TEC units, 1 TECU = $10^{16}$ electrons $m^{-2}$), which we will use in the figures.

Dautermann *et al.* (2009) computed TEC time series filtered in the acoustic frequency domain (>2.2 mHz) and identified a TEC perturbation on GPS satellites PRN31 and PRN27, starting between 14 and 20 min after the SHV explosion, consistent with the theoretical predictions for an acoustic perturbation from ground level to the peak electron density layer at ∼325 km height (Fig. 2). The TEC perturbation results from electron density variations caused by collisions between the neutral wave and the ionospheric plasma and

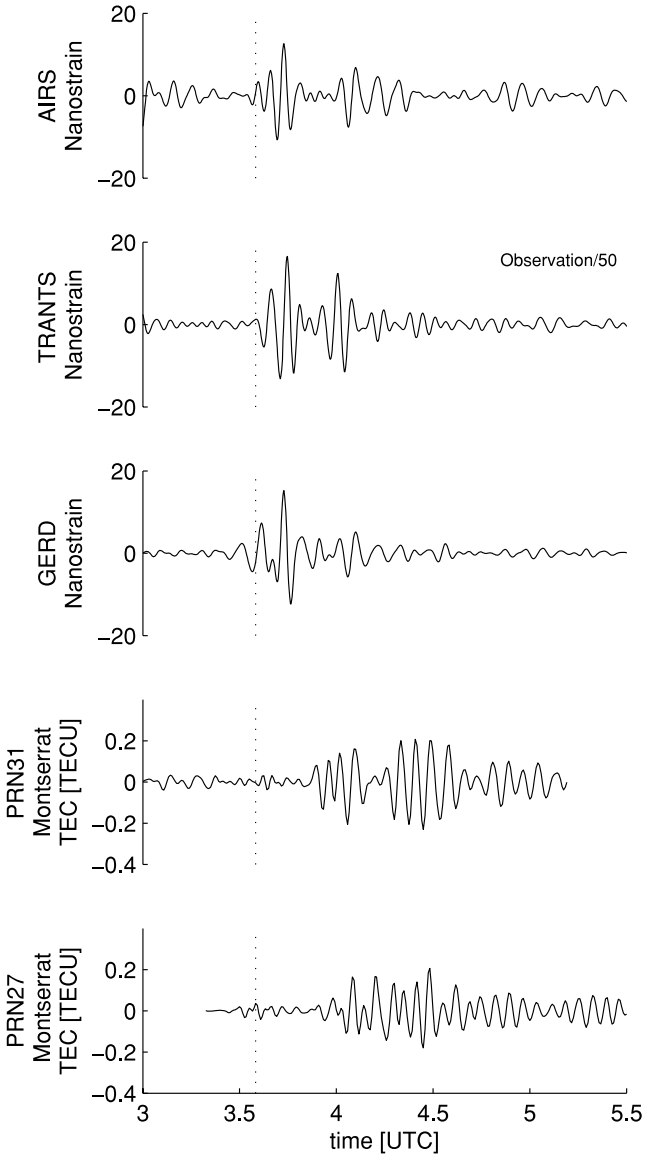


**Figure 2.** Data recorded at the three strainmeter sites (top three panels) and stacked TEC time series using the Montserrat GPS sites for PRN31 and PRN27 (bottom two panels). The data has been bandpass filtered between 2.2 and 8 mHz. A dashed line marks the time of the Soufriere Hills Volcano explosion.

can be described through the magneto-hydrodynamic state equations (see Dautermann *et al.* 2009). The ionospheric perturbation lasts for about 1.5 hr, has a spectral peak centered at 4 mHz, and an apparent propagation speed of ∼600 m $s^{-1}$, consistent with sound speed at ionospheric heights. Waveforms are well correlated among neighbouring stations but more complex than the single N-shape pulse observed by Heki (2006) or Fitzgerald (1997) after other explosions. In particular, waveforms show two wave trains separated by about 8 min, a feature previously reported after atmospheric explosions from ionospheric and surface microbarograph measurements (e.g. Harkrider 1964; Baker & Davies 1968; Tolstoy *et al.* 1971; Broche 1977; Bolt & Tanimoto 1981; Jacobson & Carlos 1994; Li *et al.* 1994) and qualitatively interpreted either as a surface reflection of the acoustic pulse (Li *et al.* 1994) or as ducted modes at the mesopause (Calais & Bernard Minster 1996).

Three Sacks–Evertson borehole dilatometers measuring volumetric strain (Sacks *et al.* 1971) were installed on Montserrat at a depth of about 180 m by the CALIPSO project (Fig. 1; Mattioli *et al.* 2004). For comparison with the TEC time series described above, we filtered the volumetric strainmeter data between 2.2 and 8 mHz (Fig. 2). Similar to the GPS-TEC data, the resulting time series show a perturbation that lasts for about 1.5 hr with two wave trains separated by about 15 min. The strain spectrograms (Figs 3a–c) show a frequency content centered around 4 mHz, with discernible power between 2 and 6 mHz, similar to that observed in the TEC data (for comparison, see TEC spectrograms in Dautermann *et al.* 2009). The strainmeter signal of interest however starts immediately after the main explosion at 3:35 UT, in contrast to the TEC perturbation, whose arrival time accounts for the propagation of the acoustic perturbation from ground level to maximum ionization height.

In spite of a waveform very similar to the other strainmeters, site TRANTS shows an amplitude that is 50 times larger than the other two sites. In addition, the explosion-related signal is preceded for about 1.5 hr by a lower amplitude signal also centered at 4 mHz (Figs 3a–c) and visible at all sites (particularly at AIRS and TRANTS). This early occurrence, along with the larger amplitude observed at coastal site TRANTS, led Mattioli *et al.* (2007) to the hypothesis that the strain signal was generated by increased ocean loading due to a tsunami triggered by pyroclastic flows, which were observed reaching the sea prior to the peak dome collapse. Mattioli *et al.* (2007) calculated that tsunami waves induced by the pyroclastic flow would reach heights of 0.2–0.5 m off-shore from TRANTS and could generate 16–88 per cent of the observed strain signal. They therefore inferred that an additional source of strain was required to explain the entire signal amplitude observed at TRANTS.

However, tsunami waves do not overlap with seismic waves in the $\omega - k$ domain considered here and hence do not couple efficiently with the solid Earth (Comer 1984). We examined in detail the raw data produced at the three strainmeter sites on a day without volanic, seismic or tsunami activity (2003 February 16). We found that the signal at three sites is similar in amplitude at frequencies above 0.5 Hz, but is amplified by about 15 times at TRANTS at frequencies between 1 and 6 mHz (16.7–2.8 min period range). This amplification could be attributed to wave action, as TRANTS is located only 40 m from the strand. An alternate explanation for the signal amplification at TRANTS might be of technical nature, possibly an incorrect gain setting in the analog-to-digital conversion and/or downsampling filtering.

The amplification at TRANTS may thus reflect either ocean loading as proposed by Mattioli *et al.* (2007), or some technical

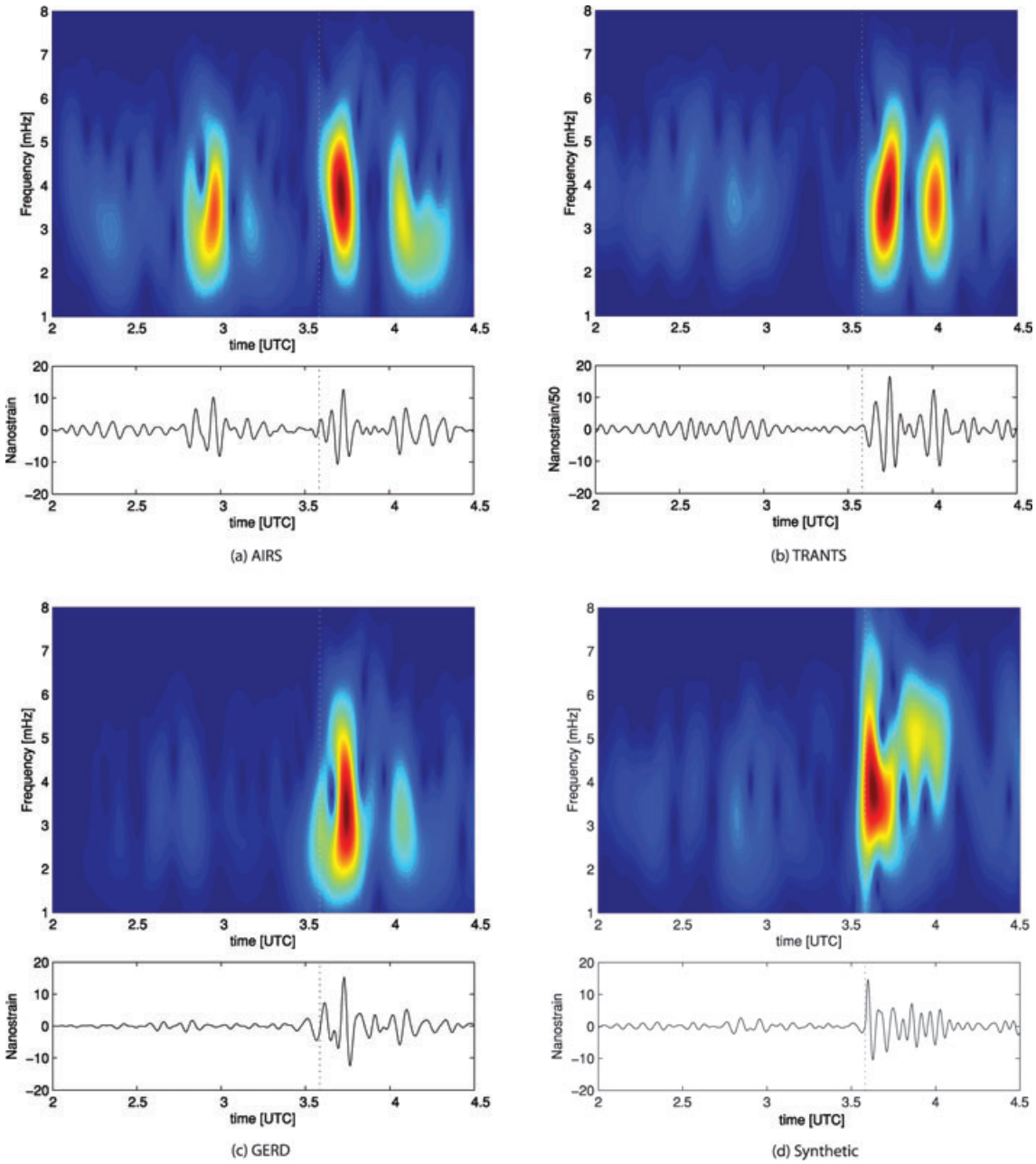


**Figure 3.** Spectrograms of the observed and synthetic strain signals using a 10 min Hamming-window with 9 min:50 s overlap. A white dashed line marks the time of the Soufriere Hills Volcano explosion.

problem in the electronics. The former interpretation is supported by TRANTS proximity to the sea and other direct observations (Alan Linde to Glen S. Mattioli, 2003, personal communication), while the latter interpretation is supported by the high level of similarity in the waveforms at all three strainmeter sites on the day of the Montserrat explosion.

Strain signals recorded after a volcanic eruption have been intrepreted as acoustic resonances in the magma chamber (Widmer & Zürn 1992). However, a resonance at 4 mHz would require the chamber to be more than 100 km in diameter (Watada 1995), inconsistent by several orders of magnitude with a chamber diameter of ∼1000 m at a depth of 6 km estimated for the source of the SHV 2003 eruption (Voight *et al.* 2006). We hypothesize that the stainmeter and ionospheric TEC signals described above were both caused by a single explosion source, with acoustic energy leakage from the atmosphere back into the solid Earth. This is supported by the similarities in waveform between TEC and strainmeter signals around 4 mHz and previous theoretical calculations by Watada (1995), Lognonné *et al.* (1998) and Lognonné (2009) showing maximum resonant coupling between atmospheric and solid Earth compressional waves at 4.4 and 3.68 mHz. Below, we quantify and test this hypothesis by simulating strain, displacement, and ionospheric perturbations using normal modes excited by an explosive source in the atmosphere at ground level.

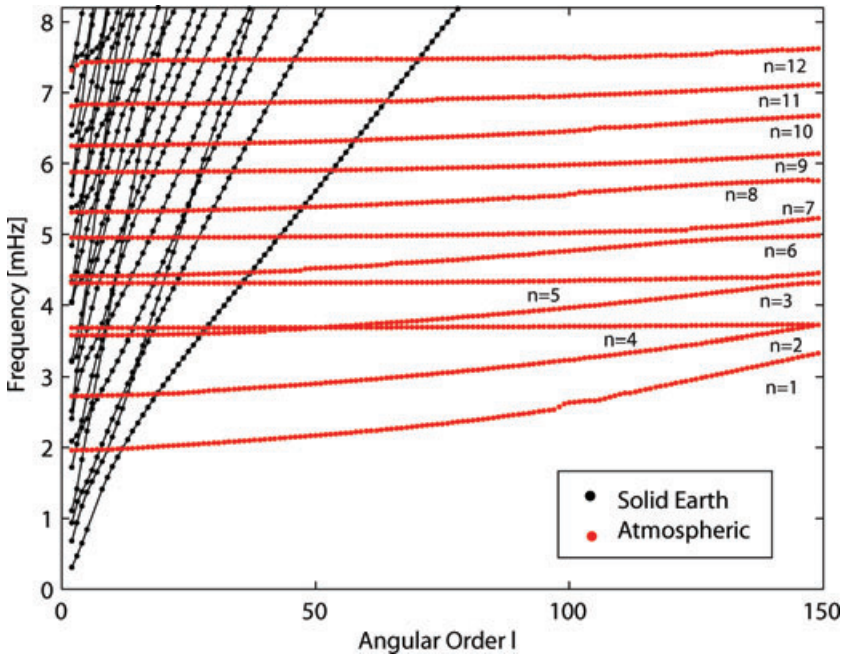


**Figure 4.** Atmospheric and solid Earth modes computed for a PREM earth model and a 500-km-thick atmosphere following the MSIS-E9-90 model. Black dots show seismic modes, red dots show atmospheric modes. Each branch corresponds to a radial order $n$ (indicated next to each atmospheric branch).

## 3 MODELLING

### 3.1 Normal modes

We simulate displacements in the atmosphere and solid Earth using a summation of the normal modes, which are the eigenfunctions to the equations of motion for the solid Earth plus atmosphere system (e.g. Lognonné *et al.* 1998; Artru *et al.* 2004). For the equilibrium mass density $\rho_0$, we use the PREM model (Dziewonski & Anderson 1981) for the solid Earth, overlain up to 500 km height with the MSIS-E-90 atmosphere model (Hedin 1987, 1991) taken at the location of the Soufriere Hills at 3.6 h UT and with the day's solar flux index values of 125.5 and 131.5 for F10.7 and F10.7a, respectively. Following Lognonné (2009), this model is expected to better account for the temporal change of the solid/atmospheric coupling efficiency with local time. As we focus on a source in the low atmosphere and long period signals, we do not account for the viscosity of the atmosphere. The method solves the Poisson equation for the gravitational potential (2) and the momentum eq. (3) for a perturbation displacement $\vec{u}$ to the equilibrium position $\vec{x}$

$$\nabla^2 V = 4\pi G\rho(\vec{x}, t) \tag{2}$$

$$\rho \frac{d^2}{\mathrm{d}t^2} u_i(\vec{x}, t) = \rho(\vec{x}, t) g_i + \frac{\partial \tau_{ij}}{\partial x_j} \tag{3}$$

($i = 1, 2, 3$) to obtain displacement $\vec{u}(\vec{x}, t)$, mass density distribution $\rho(\vec{x}, t)$, gravitational potential $V(\vec{x}, t)$ and acceleration $\vec{g} = -\nabla V$ following the method of Woodhouse (1988) for the spheroidal modes, which simultaneously integrates eqs (2) and (3) with a free boundary condition at the top of the model domain.

Since the model must account for the atmosphere with an exponentially decreasing density (artificially capped at 500 km height), we need an infinite half-space boundary condition that accounts for energy leakage at the top of the model. We incorporate this 'radiative boundary condition' using the mapping algorithms developed by Lognonné *et al.* (1998) based on a variational Rayleigh–Ritz method (e.g. Aki & Richards 2002, chapter 7.3) for the modes calculated with Woodhouse's algorithm. To obtain synthetic spectra within reasonable computation time, we calculated the modes up to a frequency of 8 mHz and maximum angular order $l = 150$ (Fig. 4).

From the attenuation coefficient $\gamma$ of each mode, we compute a dimensionless quality factor $Q$ that compares the time constant of the attenuation to the oscillation period of each mode [which decays as $\exp(-\gamma t) = \exp(-Re(\sigma)t/(2Q))$ with $\sigma$ the angular frequency]. The larger the quality factor, the smaller the mode damping. Fig. 5 shows that the atmospheric mode branch $n = 3$, with frequency ranging from 3.67 to 3.72 mHz, is the least attenuated, followed by the $n = 5$ and 7 branches. We note here that the radial order is the one for the complete system and that these three branches correspond, respectively, to the atmosphere fundamental mode and its two overtones. Higher overtones have a very low $Q$ and are not trapped. Fig. 5 shows that modes $n = 3, 5, 7$ carry the bulk of the energy released by the explosion in the atmosphere, consistent with the frequency content of the atmospheric perturbation observed after the SHV and other atmospheric explosions.

### 3.2 Source energy and mode summation

To generate displacements, one needs the excitation strength, quantified by the source moment. Since the source is an atmospheric explosion associated to the (permanent) collapse of SHV peak dome, we use a Heaviside source function and an isotropic moment $M$, related to the energy release $E$ by

$$E = \frac{\Delta P}{2\mu} M, \tag{4}$$

where $\mu = 4 \times 10^9$ Pa is the shear modulus for andesite (Voight *et al.* 2006) and $\Delta P = 12 \times 10^6$ Pa the pressure release, as reported

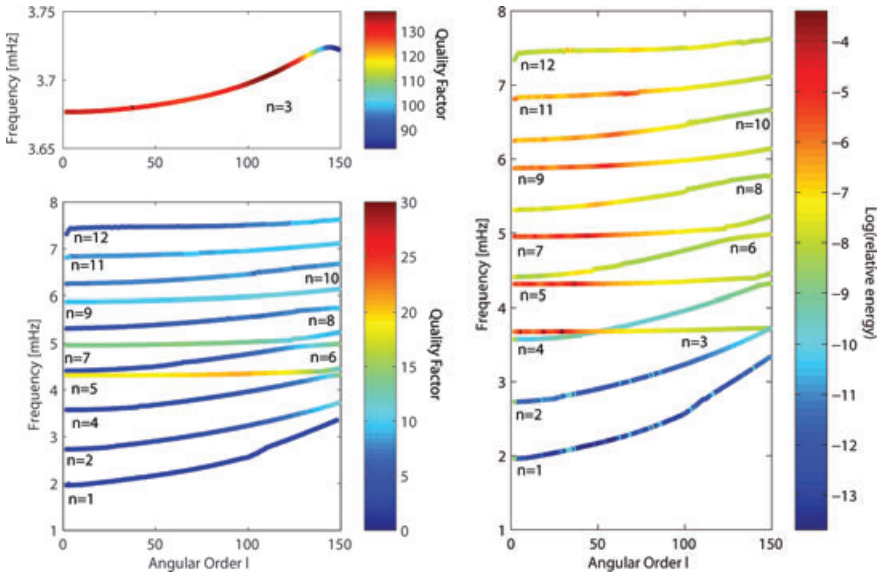


**Figure 5.** Left-hand panels: quality factor ($Q$) for the atmospheric modes. High values of the quality factor correspond to low damping. Mode branch $n = 3$ is separated out in the top left panel, since $Q$ is one order of magnitude higher for this branch. Right-hand panel: normalized energy for the atmospheric modes. The energy is normalized with respect to the seismic mode of maximum energy. Colour scale shows the logarithm of that normalized energy.

by Herd *et al.* (2005) during the explosion associated with the SHV peak dome collapse. The total energy release is the sum of the acoustic and seismic energy released by the explosion. We use an acoustic energy of $1.53 \times 10^{10}$ J as estimated by Dautermann *et al.* (2009) from GPS-TEC data. We estimate the seismic energy following Kanamori *et al.* (1993):

$$E_{\text{Seismic}} = 4\pi r^2 \rho c Q(r)^2 \int v^2(t)\,\mathrm{d}t, \tag{5}$$

where $r$ is distance from the source, $\rho$ the average mass density of the volcanic edifice (taken as 2100 kg m$^{-3}$ from Voight *et al.* 2006), $c$ the $S$-wave velocity $c = \sqrt{\mu/\rho}(\mu = 4 \times 10^9$ Pa), $Q(r)$ the attenuation function from Kanamori *et al.* (1993). We compute $v(t)$ from the strain data using

$$v(t) = \frac{\Delta L}{\Delta t} = \frac{L}{3\Delta t} \times \text{Volumetric Strain} \tag{6}$$

with $L = \sqrt[3]{V_0}$ where $V_0$ is the volume of the strainmeter. Using the above equations, we find that the seismic energy varies little over all frequencies below 1 Hz and has an average value of $E_{\text{Seismic}} = 5.49 \times 10^8$ J, two orders of magnitude smaller than the acoustic energy reported in Dautermann *et al*. (2009). We therefore neglect the seismic energy contribution in the source moment calculation. Eq. (4) then leads to a source moment of $1.02 \times 10^{13}$ N m.

We then sum all computed modes following Lognonné's (1991) rule, accounting for attenuation arising from energy leakage at the top of the atmosphere and in the solid Earth

$$\vec{u}(\vec{x}, t) = \sum_{i,n,l,m} Real\left[\epsilon_{n,l,m,i,i}(\vec{x}_s) M_{ii} \vec{u}_{n,l,m}(\vec{x}) \frac{1 - e^{i\sigma_{n,l}t}}{\sigma_{n,l}^2}\right] \tag{7}$$

where $n$, $l$, $m$ is radial, angular and azimuthal orders of the normal modes, respectively, $M_{ii}$ is moment tensor (isotropic here) and $\epsilon_{n,l,m,i,j}$ is strain components of mode $(n, l, m)$ and $\sigma_{n,l}$ the eigenfrequency. Note that both the eigenfrequencies and eigenmodes are complex. This leads to displacement $\vec{u}(\vec{x}, t)$ at any point in the model domain. We then compute volumetric strain $\Delta V$ by differencing the model displacement over the dimensions of the borehole strainmeter.

### 3.3 Ionospheric coupling

We compute electron density perturbations assuming that ionospheric charged particles follow the motion of neutral gas through collision interactions (Davies & Archambeau 1998). Details of the methodology are reported in Dautermann *et al.* (2009; see also Kherani *et al.* 2008). Collision interactions are described via the Navier–Stokes equation of magneto-hydrodynamics

$$\rho_e \frac{\mathrm{d}\vec{v}_e}{\mathrm{d}t} = -\nabla p + \rho_e \vec{g} + Ne(\vec{v}_e \times \vec{B}) - \rho_e \nu_{en}\left(\vec{v}_e - \frac{\mathrm{d}\vec{u}}{\mathrm{d}t}\right). \tag{8}$$

From this, we compute the electron plasma velocity $v_e$ using a finite difference scheme. Input parameters are the hydrostatic pressure gradient $\nabla p(z)$ from our earth model, electron mass density $\rho_e$, electron number density $N$ from the International Reference Ionosphere (Bilitza 2001), electron charge $e$, Earth's magnetic field $\vec{B}$ from the International Geomagnetic Reference Field IGRF-10 (Maus & Macmillan 2005), and the neutral–electron collision frequency $\nu_{en}$ based on the equations given by Schunk & Nagy (1980) for the two most abundant neutral gasses at ionospheric altitudes, neutral oxygen and molecular nitrogen. Neutral velocity $\vec{u}$ is derived from the normal mode summation technique presented above. Both the electric field and magnetic field perturbation are neglected here. These simplifications are not expected to modify the results to the first order.

To obtain the electron density perturbation, we integrate the continuity equation for the charge density from the explosion time to the observation time $t$

$$\delta N(\vec{r}_I, t) = -\frac{\partial N}{\partial z}\int_{t_{\text{explosion}}}^{t} v_{e,z}(\vec{r}_I, \hat{t})\mathrm{d}\hat{t} - N(z)\int_{t_{\text{explosion}}}^{t} \nabla \cdot \vec{v}_e(r_I, \hat{t})\mathrm{d}\hat{t}. \tag{9}$$

We integrate the electron density perturbations $\delta N$ along the satellite to receiver ray path, accounting for satellite motion, in order to obtain a simulated TEC value comparable to the observed one. The computational cost of eq. (9) is high, because the second integral contains the divergence of the velocity, which requires summing all normal modes six times to obtain the complete spatial derivative. To minimize computational burden, we perform this calculation along the satellite-receiver line of sight at 10 points distributed through the bulk of the electron density concentration at altitudes of 250, 300, 310, 320, 325, 330, 340, 350, 375, 400 and 450 km.

### 3.4 Results

Fig. 6 shows the synthetic and observed volumetric strain and TEC signals, zero-phase band-pass filtered (Butterworth filter) between 2.2 mHz (acoustic cut-off frequency, e.g. Beer 1974) and 8 mHz (Nyquist frequency of the GPS-TEC signal for a 30 s sampling rate) to isolate the acoustic component. We used average background noise from observed time series before the eruption to avoid filter artefacts caused by the abrupt, step-like, increase in strain that is generated by our model immediately after 3:35 UT. The simulated volumetric strain signals are identical at the 3 strainmeters. Initial rise in model strain starts at 3:35 UT and falls off after 4:10 UT in accordance with the observations. Simulated waveforms for the first wave train match the data well, except for the larger amplitude initial peak in the model. The model reproduces the double wave train visible in the data, particularly distinct at site AIRS. However, at this site, the second wave train in the model arrives earlier than observed. Model amplitudes are reasonably consistent with the observations at sites AIRS and GERD, although in both cases slightly lower. Simulated amplitude at coastal site TRANTS is 50 times lower than observed, which, as discussed above, could result from a coincidental tsunami (the pyroclastic flow induced ocean loading would have to amplify the strain signal and also precisely conserve the waveform of an atmospheric explosion) or from a technical issue at the A/D recorder.

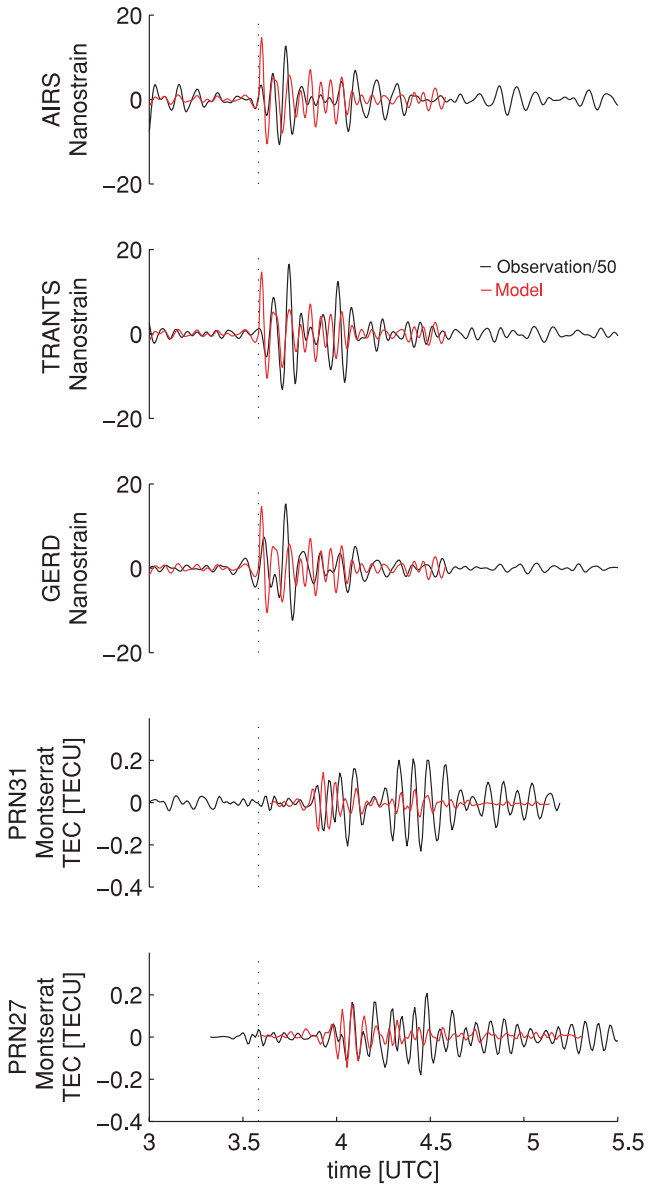


**Figure 6.** Data recorded at the three strainmeter sites (top three panels, black) and stacked TEC time-series using the Montserrat GPS sites for satellites PRN31 and PRN27 (bottom two panels, black) compared to model synthetics (red). Note that the observed strain signal amplitude at site TRANTS has been divided by 50 to match the synthetics.

The spectrogram of the synthetic strain time-series (Fig. 3d) shows the two wave trains with 15–20 min duration and separated by about 5.5 min, in reasonable agreement with the observations. The first pulse starts at the time of the explosion and is centred at 3.5 mHz while the second one is centered at 4.5 mHz. The spectral power of the synthetics agrees best with site TRANTS, where strain data show two pulses of equivalent magnitude.

Arrival times of the TEC perturbation are well reproduced by the model, as well as the signal amplitude and its attenuation as a function of distance to the source (Fig. 6). The model reproduces the double wave train observed in the TEC time-series at near field sites HOUE through MVO1 (Fig. 7) and predicts the attenuation of the second pulse as the distance to the source increases, consistent with observations. Maximum modelled TEC amplitudes in the far field, however, are 12 per cent (BGGY) and 61 per cent (CRO1) smaller than observed. Amplitudes of the second wave train in the model are about 50 per cent smaller than observed at all sites except in the very near field at HOUE. This is likely related to local heating of the atmosphere by the plume, a process that decreases density and hence results in a larger signal amplitude.

## 4 DISCUSSION

Although there are mismatches between modelled and observed signals, their duration, waveform characteristics and arrival times match reasonably well. The overall agreement in amplitude between modelled and observed signals indicates that (1) seismic energy in the frequency band considered here is small compared to acoustic energy and (2) the acoustic energy estimate from Dautermann *et al.*'s (2009) ray tracing model was accurate.

Mismatches between model and observed TEC signals may result from neglecting winds as well as temperature and density deviations from the MSIS-E-90 atmosphere model, both of which have been shown to impact the timing and propagation paths of atmospheric acoustic waves (e.g. Argo *et al.* 1995). In addition, the point source used here is likely an oversimplification of a longer and more complex source function, with a moment that may not be perfectly isotropic (e.g. Brodsky *et al.* 1999). Another limitation in our model is the summation of modes only up to angular order $l = 150$, implying that some of the energy within the bandwidth considered

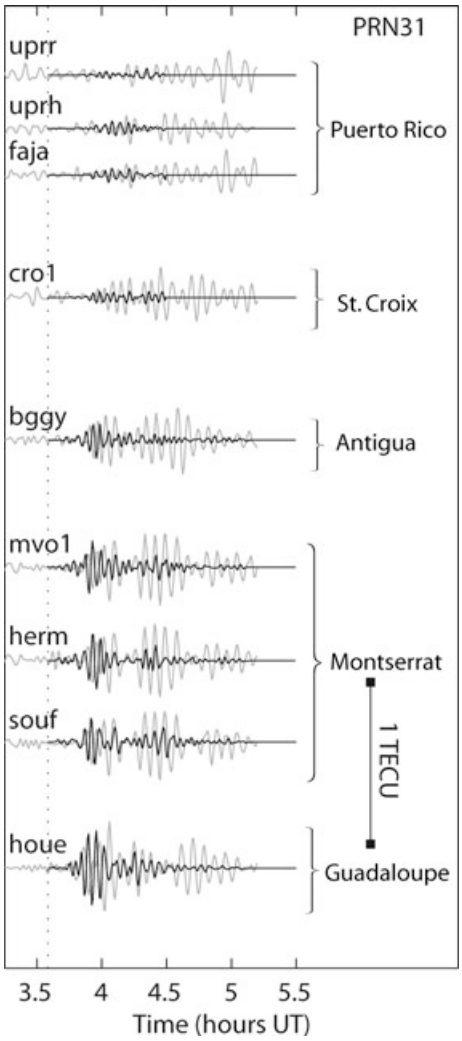


**Figure 7.** Synthetic TEC computed using normal mode summation shown for satellite PRN31 and sorted by distance of the SIP to the SHV at explosion time. The observed TEC time-series are shown in grey in the background. Time-series are grouped in clusters of nearby sites.

here is not included in the summation. This may explain the larger differences in amplitude between model and observations at sites far from the source compared with sites at closer distances, because higher angular orders are attenuated by the atmospheric viscosity as well as by the finite size of the source. Finally, additional complexity in both the volumetric strain and TEC signals may arise because of smaller, secondary explosions not taken into account here which occurred after the primary moment release at 3:35 UT, as well as deformation processes at shallow levels within the magma-conduit system not modelled here.

It is remarkable that a point source excitation at ground level gives rise to two wave trains in both the TEC and strain signals. This result indicates that earlier interpretations of similar observations as a reflection of the initial pulse (Li *et al.* 1994) or as the result of ducted modes at the mesopause (Calais & Bernard Minster 1996) may have been incorrect since both require a source at or near the mesopause. As shown on Fig. 8, the double wave train results from the beat of the dominant atmospheric modes $n = 3, 5, 7$ and is therefore an intrinsic property of the atmospheric medium rather than a source or a propagation effect.

As a corollary, the fact that a similar double wave train is recorded at borehole strainmeters indicates that part of the strain perturbation is due to energy leakage from the atmosphere to the solid Earth. To further illustrate this effect, we split the synthetic strain into its atmospheric and seismic mode components, which we compute for an atmospheric source at the actual height of the SHV and for a source located 100 m below the ground surface. Fig. 9 shows that solid Earth modes are excited similarly by the two sources and result in a strain waveform with shorter duration and absence of a double wave train. Atmospheric modes exhibit the double wave train for a source located in the atmosphere, but not for an underground source, which also results in a strain amplitude 1000 times smaller. We can infer from this that the observed strain signal requires a contribution from atmospheric modes excited by an atmospheric explosion in order to produce the long lasting strain variations and the double wave train observed.

The fact that this double wave train was not reproduced in the ray tracing model of the SHV explosion by Dautermann *et al.* (2009) may be due to the approximation to the atmospheric dispersion relation used in that study. The spectral method used here, with the summation of the eigenfunctions, includes the unapproximated dispersion relation, as the frequency content changes with the attenuation time in a manner unique to each mode (according to the complex part of the eigenfrequency). In addition, the first and second overtones described above are leaky modes and only the fundamental mode has a high enough $Q$ to be well approximated by ray theory.

The seismic and acoustic energy released by the SHV explosion explain most of the signal observed at the strainmeters but may not be the only contributing mechanism, as shown by the pre-explosion signal visible at 2:45 UT (Fig. 3a, particularly visible at site AIRS). These early perturbations were inferred to result from pyroclastic flows observed on the volcano flank that reached the sea several hours before the explosive dome collapse and triggered a tsunami (Mattioli *et al.* 2007). Tsunami-induced ocean loading propagating to the strainmeters through poro-elastic stresses may have contributed part of the observed signal.

## 5 CONCLUSIONS

We have shown that the complex signal observed at borehole strainmeters and in GPS-TEC following the SHV dome collapse can be modelled by a single explosive source in the atmosphere. Similarities in waveforms between strainmeter and GPS-TEC time-series, in particular the double wave train reported here and after several other instances of explosion-triggered atmospheric or ionospheric perturbations, result from the superposition of the dominant atmospheric modes $n = 3, 5, 7$ that, in turn, trigger resonant coupling with the solid Earth at 4 mHz.

The results presented here highlight the importance of the dispersion of the acoustic pulse, the main process responsible for the long duration wave trains observed after explosions, shallow earthquakes, or other sources that trigger acoustic atmospheric perturbations. As a result of dispersion, fully accounted for in the normal mode summation approach used here, an isotropic point explosion can cause atmospheric oscillations with complex waveforms (e.g. double wave train) that persist for tens of minutes after an event.

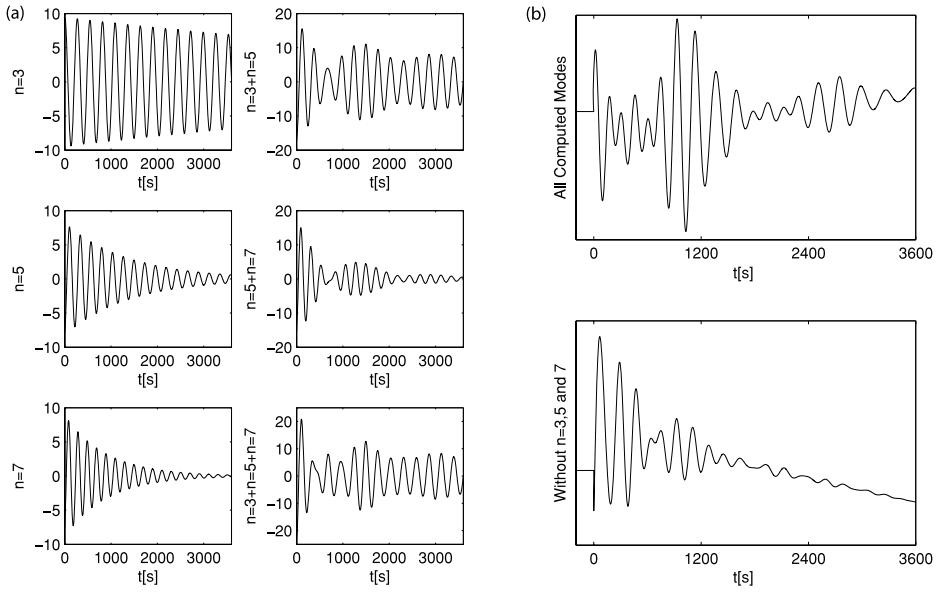


**Figure 8.** (a) Left-hand panels: displacement (normalized) for the three least attenuated atmospheric mode branches ($n = 3$, 5, 7, see Fig. 5). Right-hand panels: summation of these modes showing that the double wave train observed in the data results from the beat of the dominant atmospheric modes. The simulations shown here correspond to angular order $l = 28$, chosen because it is one of the modes that allows energy transfer from the solid Earth to the atmosphere. (b) Summation at a distance of 0.5° from the source with all modes (top panel) and without the three most strongly coupled mode branches $n =$ 3, 5 and 7 (bottom panel). A pronounced double wave train is visible when those three mode branches are included.

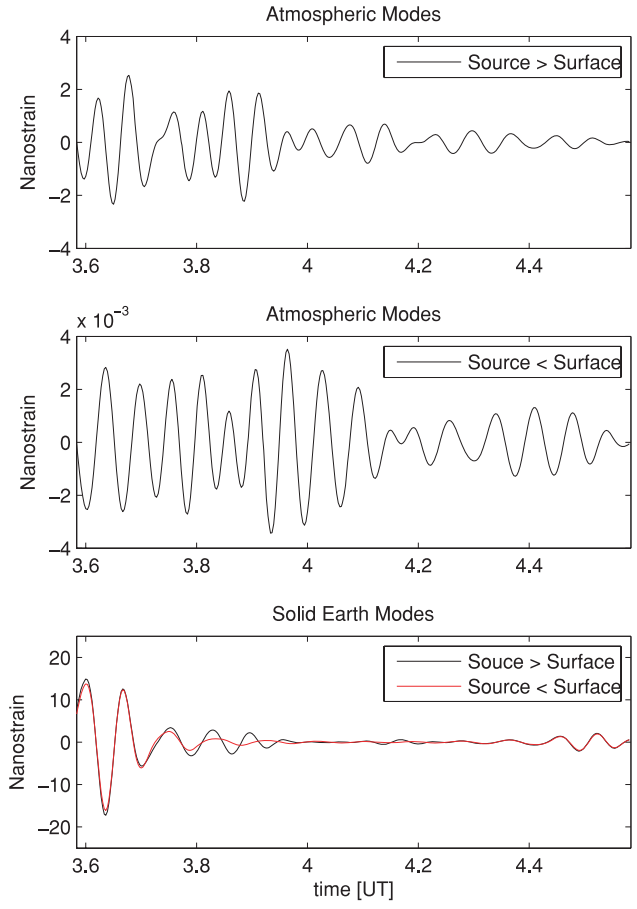


**Figure 9.** Model volumetric strain generated for an isotropic point source located within the atmosphere at 1 km altitude (top and bottom red traces), and the same point source located 100 m below the surface (middle and bottom black traces). Note the scale difference between panels.

## ACKNOWLEDGMENTS

We thank the NSF-EAR CD and IF programs for continued support of the CALIPSO facility (NSF-IF-0523097 and NSF-IF-0732728) and analysis of data derived from it (NSF-CD-0607782). PL thanks CNES for their support to his group's ionospheric studies, IPGP contribution 2555. We thank Emile Okal and reviewers Jeffrey B. Johnson and Giovanni Occhipinti for their insightful comments.

## REFERENCES

Afraimovich, E.L., Perevalova, N.P., Plotnikov, A.V. & Uralov, A.M., 2001. The shock-acoustic waves generated by earthquakes, *Ann. Geophys.,* **19,** 395–409.

Aki, K. & Richards, P.G., 2002. *Quantitative Seismology,* 2nd edn, University Science Books, Sausalito, CA, ISBN 0-935702-96-2, 704 pp.

Argo, P. *et al.*, 1995. The detection and recognition of underground nuclear explosions, *Surv. Geophys.,* **16,** 495–532.

Artru, J., Lognonné, P. & Blanc, E., 2001. Normal modes modelling of post-seismic ionospheric oscillations, *Geophys. Res. Lett.,* **28,** 697–700.

Artru, J., Farges, T. & Lognonné, P., 2004. Acoustic Waves generated from seismic surface waves: propagation properties determined from doppler sounding observations and normal-mode modeling, *Geophys. J. Int.,* **158,** 1067–1077.

Baker, D.M. & Davies, K., 1968. Waves in the ionosphere produced by nuclear explosions, *J. geophys. Res.,* **73,** 448–451.

Beer, T., 1974. *Atmospheric Waves,* Wiley, New York.

Bilitza, D., 2001. International Reference Iononosphere 2000, *Radio Sci.,* **36,** 261–276.

Bolt, B. & Tanimoto, T., 1981. Atmospheric oscillations after the May 18, 1980 eruption of Mount St. Helens, *EOS, Trans. Am. geophys. Un.,* **62,** 529–530.

Broche, P., 1977. Propagation des Ondes acoustico-gravitationelles excitées par des explosions, *Annales Geophysicae,* **33**(3), 281–288.

Brodsky, E.E., Kanamori, H. & Sturtevant, B., 1999. A seismically constrained mass discharge rate for the initiation of the May 18, 1980 Mount St. Helens eruption, *J. geophys. Res.,* **104,** 29 387–29 400.

Calais, E. & Bernard Minster, J., 1996. GPS Detection of ionospheric perturbations following a space shuttle ascent, *Geophys. Res. Lett.,* **23,** 1897–1900.

Calais, E., Bernard Minster, J., Hofton, M. & Hedlin, M., 1998. Ionospheric signature of surface mine blasts from global positioning system measurements, *Geophys. J. Int.,* **132,** 191–202.

Comer, P., 1984. Tsunami generation: a comparison of traditional and normal mode approaches, *Geophys. J. R. astr. Soc.,* **77,** 29–41.

Dautermann, T., Calais, E. & Mattioli, G.S., 2009. GPS Detection, modeling and energy estimation of the ionospheric wave caused by the 2003 explosion of the Soufriere Hills Volcano, Montserrat, *J. geophys. Res.,* **114,** B02202, doi:10.1029/2008JB005722.

Davies, J.B. & Archambeau, C.B., 1998. Modeling of atmospheric and ionospheric disturbances from shallow seismic sources, *Phys. Earth planet. Interiors,* **105,** 183–199.

Ducic, V., Artru, J. & Lognonné, P., 2003. Ionospheric remote sensing of the Denali earthquake Rayleigh surface waves, *Geophys. Res. Lett.,* **30**(18), 8-1–8-4.

Dziewonski, A.M. & Anderson, D.L., 1981. Preliminary reference earth model, *Phys. Earth planet. Inter.,* **25,** 297–356.

Fitzgerald, T.J., 1997. Observations of total electron content perturbations on GPS signals caused by a ground level explosion, *J. Atmos. Terrestrial Phys.,* **59,** 829–834.

Harkrider, D.G., 1964. Theoretical and observed acoustic-gravity waves from explosive sources in the atmosphere, *J. geophys. Res.,* **69,** 5295–5305.

Hedin, A.E., 1987. MSIS-86 thermospheric model, *J. geophys. Res.,* **92,** 4649–4662.

Hedin, A.E., 1991. Extension of the MSIS thermosphere model into the middle and lower atmosphere, *J. geophys. Res.,* **96,** 1159–1172.

Heki, K., 2006. Explosion energy of the 2004 eruption of the Asama Volcano, central Japan, inferred from ionospheric disturbances, *Geophys. Res. Lett.,* **33**, L14303, doi:10.1029/2006GL026249.

Herd, R.A., Edmonds, M. & Bass, V.A., 2005. Catastrophic lava dome failure at Soufriere Hills Volcano, Montserrat, 12-13 July 2003, *J. Volc. Geotherm. Res.,* **148,** 234–252.

Jacobson, A.R. & Carlos, R.C., 1994. Observations of acoustic-gravity waves in the thermosphere following Space Shuttle ascents, *J. Atmos. Terrestrial Phys.,* **56,** 525–528.

Kanamori, H. & Mori, J., 1992. Harmonic excitation of mantle Rayleigh waves by the 1991 eruption of Mount Pinatubo, Philippines, *Geophys. Res. Lett.,* **19**(7), 721–724.

Kanamori, H., Mori, J., Hauksson, E., Heaton, T.H., Hutton, L.K. & Jones, L.M., 1993. Determination of earthquake energy release and ML using TERRAscope, *Bull. seism. Soc. Am.,* **83**(2), 330–346.

Kanamori, H., Mori, J. & Harkrider, D.G., 1994. Excitation of atmospheric oscillations by volcanic eruptions, *J. geophys. Res.,* **99**(18), 21 947–21 961.

Kherani, E.A., Lognonné, P., Kamath, N., Crespon, F. & Garcia, R., 2008. Response of the Ionosphere to the seismic trigerred acoustic waves: electron density and electromagnetic fluctuations, *Geophys J. Int.,* **176**(1), 1–13.

Klobuchar, J.A., 1985. Ionospheric time delay effects on earth space propagation, in *Handbook of Geophysics and the Space Environment*, pp. 1084–1088, ch. 10.8, ed. Jursa, A.S., U.S. Air Force, Washington, D.C.

Kobayashi, N., 2007. A new method to calculate normal modes, *Geophys. J. Int.,* **168,** 315–331.

Li, Y.Q., Jacobson, A.R., Carlos, R.C., Massey, R.S., Taranenki, Y.N. & Wu, G., 1994. The blast wave of the Shuttle plume at ionospheric heights, *Geophys. Res. Lett.,* **21,** 2737–2740.

Lognonné, P., 1991. Normal modes and seismograms in an anelastic rotating Earth, *J. geophys. Res.,* **96,** 20,309–20,319.

Lognonné, P., 2009. Seismic waves from atmospheric sources and atmospheric/ionospheric signatures of seismic waves, in *Infrasound Monitoring for Atmospheric Studies,* ed. Le Pichon, A., Springer, New York.

Lognonné, P., Clévédé, E. & Kanamori, H., 1998. Computation of seismograms and atmospheric oscillations by normal-mode summation for a spherical earth model with realistic atmosphere, *Geophys. J. Int.,* **135,** 388–406.

Lognonné, P. *et al.*, 2006. Ground-based GPS imaging of ionospheric post-seismic signal, *Planet. Space. Sci.,* **54,** 528–540.

Mattioli, G.S. *et al.*, 2004. Prototype PBO Instrumentation of CALIPSO Project Captures World-Record Lava Dome Collapse on Montserrat Volcano, *EOS, Trans. Am. Geophys. Un.,* **85,** 317–323.

Mattioli, G.S. *et al.*, 2007. Unique and remarkable dilatometer measurements of pyroclastic flow generated tsunami waves, *Geology,* **35**(1), 25–28.

Maus, S. & Macmillan, S., 2005. International geomagnetic reference field—the tenth generation, *Earth Planets Space,* **57**(12), 1135–1140.

Mazzella, A.J., Holland, E.A., Andreasen, A.M., Andreasen, C.C., Rao, G.S. & Bishop, G.J., 2002. Autonomous estimation of plasmasphere content using GPS measurements, *Radio Science,* **37,** 4–1.

Occhipinti, G., Lognonné, P., Kherani, E.A. & Hébert, H., 2006. Three-dimensional waveform modeling of ionospheric signature induced by the 2004 Sumatra tsunami, *Geophys. Res. Lett.,* **33**(20104).

Sacks, I., Suyehiro, S., Evertson, D.W. & Yamagishi, Y., 1971. Sacks–Evertson Strainmeter, its installation in Japan and some preliminary results concerning strain steps, *Papers Met. Geophys.,* **22**(3–4), 195–208.

Sardon, E., Rius, A. & Zarraoa, N., 1994. Estimation of the transmitter and receiver differential biases and the ionospheric total electron content from Global Positioning System observations, *Radio Sci.,* **29**(3), 577–586.

Schunk, R.W. & Nagy, A.F., 1980. Ionospheres of the terrestrial planets, *Rev. Geophys. Space Phys.,* **18,** 813–852.

Tolstoy, I. & Lau, J., 1971. Generation of long internal gravity waves in waveguides by rising buoyant air masses and other sources, *Geophys. J.,* **26,** 295–310.

Voight, B. *et al.*, 2006. Unprecedented pressure increase in deep magma reservoir triggered by lava-dome collapse, *Geophys. Res. Lett.,* **33,** L03312, doi:10.1029/2005GL024870.

Watada, S., 1995. Part 1: near source acoustic coupling between the atmosphere and the solid earth during volcanic erruptions, *PhD thesis*, California Institute of Technology.

Widmer, R. & Zürn, W., 1992. Bichromatic excitation of long-period Rayleigh and air waves by the Mount Pinatubo and El Chichon volcanic eruptions, *Geophys. Res. Lett.,* **19,** 765–768.

Woodhouse, J.H., 1988. The calculation of Eigenfrequencies and Eigenfunctions of the free oscillations of the Earth and the Sun, in *Seismological Algorithms,* pp. 321–370, ed. D.J. Dornboos, Academic Press, New York.